



Assessment of relative dispersion in the Gulf of Tonkin using numerical modeling and HF radar observations of surface currents

Manh Cuong Tran^{a,b,e,*}, Alexei Sentchev^{a,e}, Stefano Berti^c, Nadia K. Ayoub^{d,e}, Tung Nguyen-Duy^{d,e}, Nguyen Kim Cuong^f

^a Laboratory of Oceanology and Geosciences, UMR 8187, CNRS, Univ. Littoral Côte d'Opale, Univ. Lille, IRD, 62930, Wimereux, France

^b Center for Oceanography (CFO), Vietnam Administration of Seas and Islands (VASI), 8 Phao Dai Lang, Dong Da, Hanoi, Viet Nam

^c Univ. Lille, ULR 7512, Unité de Mécanique de Lille Joseph Boussinesq (UML), 59000, Lille, France

^d LEGOS, UMR5566, IRD, CNES, CNRS, Université de Toulouse, 31400, Toulouse, France

^e LOTUS Laboratory, University of Science and Technology of Hanoi, Vietnam Academy of Science and Technology, Hanoi, Viet Nam

^f VNU University of Science, Vietnam National University, 334 Nguyen Trai, Thanh Xuan, Hanoi, Viet Nam

ARTICLE INFO

Keywords:

Relative dispersion
Scale of motion
HF radar measurements
Numerical modeling
Gulf of Tonkin

ABSTRACT

Particle pair statistics from synthetic drifter trajectories reconstructed from realistic, high-resolution numerical simulations (SYMPHONIE model) and HF radar velocity measurements are used to investigate the dispersion properties in the Gulf of Tonkin (GoT). This study takes an approach based on two-particles statistics providing the relative dispersion, relative diffusivity and Finite Size Lyapunov Exponent (FSLE) estimates. In the GoT, the relative dispersion follows the predictions from the theory of two-dimensional turbulence with two inertial subranges identified in the kinetic energy spectrum with the spectral slopes $-5/3$ and -3 . The time evolution of dispersion shows an exponential growth during 5–8 days, followed by a power law regime during the next 6–20 days. Fixed-length indicators from the relative diffusivity and the FSLE reveal a local dispersion at large and intermediate scales (above Rossby radius of deformation) and non-local dispersion in sub-mesoscale range (below Rossby radius of deformation). The effect of river runoff on the local hydrodynamics and dispersion processes is assessed using the numerical model simulations without river discharge. The results show that in the model, the river plume, when present, highly impacts the Lagrangian statistics. High gradients of buoyancy reinforce the sub-mesoscale circulation in a large region along the Vietnamese coast and modify the scales and intensity of turbulent dispersion. However, a clear change of dispersion regime in the sub-mesoscale range is not identified, suggesting that the mesoscale circulation in the GoT largely governs particle spreading even at small scale.

1. Introduction

Transport and dispersion processes in the ocean have practical importance since they play a major role in the functioning of marine ecosystems by carrying physical and chemical quantities such as heat, salt, nutrients, as well as biological relevant tracers, matter and marine debris. For example, in the North Sea, the transport of the flatfish larvae from the spawning areas to the nurseries and mortality rate are heavily impacted by the hydrodynamics processes and the environmental factors (Lacroix et al., 2013). In the coastal zone, the knowledge of transport properties is even more important for assessing the dispersal of anthropogenic pollutant tracers released accidentally (Corrado et al.,

2017). Mapping the transport pathways of materials advected by ocean currents is of great interest for understanding the interconnection between geographical regions (Haza et al., 2010; van Sebille et al., 2011, 2015), physical and relevant biogeochemical processes (d'Ovidio et al., 2015). However, prediction of the Lagrangian transport remains challenging since the oceanic flow is turbulent in a wide range of spatial and temporal scales. The oceanic coherent structures, which we refer to as jets, eddies, fronts, arise from multi-scale interactions of physical processes in the ocean and at its interfaces with the atmosphere and the continent. The instabilities of these structures, due to the flow turbulence or episodic forcing (e.g., wind), result in chaotic motions and may dictate the transport statistics (Haza et al., 2016).

* Corresponding author. Laboratory of Oceanology and Geosciences, UMR 8187, CNRS, Univ. Littoral Côte d'Opale, Univ. Lille, IRD, 62930, Wimereux, France.
E-mail address: manh-cuong.tran@univ-littoral.fr (M.C. Tran).

<https://doi.org/10.1016/j.csr.2022.104784>

Received 9 March 2022; Received in revised form 26 May 2022; Accepted 9 June 2022

Available online 11 June 2022

0278-4343/© 2022 Elsevier Ltd. All rights reserved.

Lagrangian framework is naturally linked to the investigation of transport since the Lagrangian observations track the fluid parcels and sample the spatiotemporal evolution of their properties rather than measuring them at a fixed point in the Eulerian approach (Essink et al., 2019). Trajectory maps can provide the details of the circulation and dispersion of materials in the flow field. Since an individual trajectory in the turbulent flow field is largely unpredictable and depends strongly on the initial conditions, the ensemble average over many trajectories is needed to provide the statistical description of the flow field (LaCasce, 2008; Essink et al., 2019).

Characteristics of the oceanic turbulent flow based on the Lagrangian approach have been described in many studies, e.g., in the North Atlantic (Lumpkin & Elipot, 2010), in the South Atlantic, (Berti et al., 2011), in the Nordic Seas (Koszalka et al., 2009), in the Gulf of Mexico (LaCasce & Ohlmann, 2003; D'Asaro et al., 2018), and in the Mediterranean Sea (Haza et al., 2010; Schroeder et al., 2011, 2012; Hernández-Carrasco et al., 2018a). These studies aimed to explore how pollutants or biological tracers disperse in the marine environment and how the energy is transferred across scales of motion. The relative dispersion, which might be estimated from the mean squared separation of particle pairs, is used to characterize the underlying turbulent flow field. Among the Lagrangian statistics, pair dispersion gains importance since the spreading rate of pairs of particles is sensitive to the amount of energy distribution within different scales. The spreading of particle pairs depends, in principle, on the velocity difference at the length scale corresponding to the pair separation distance (Lumpkin & Elipot, 2010). Therefore, the statistics based on relative dispersion are useful for the assessment of mixing in the turbulent flow field at small and intermediate scales and can characterize the most important physical processes controlling the underlying fluid motions (Meyerjürgens et al., 2020).

The relationship between the oceanic turbulent flow and the relative dispersion statistics has been extensively discussed (see, e.g., LaCasce, 2008; Foussard et al., 2017; Berti and Lapeyre, 2021). It was shown that the dispersion properties can be theoretically predicted from the kinetic energy spectrum, $E(k) \sim k^{-\beta}$, of the underlying flow field. Specifically, the relative dispersion can be either local if $1 < \beta < 3$, or non-local, in the case of $\beta \geq 3$. In a number of studies using the relative dispersion statistics (Koszalka et al., 2009; Lumpkin & Elipot, 2010; Poje et al., 2014; van Sebille et al., 2015; Sansón et al., 2016; Beron-Vera and LaCasce 2016; Corrado et al., 2017; Essink et al., 2019), the geographic dependency of the stirring regime is found across different ocean regions. Contradictory results in some regions have been reported revealing a non-local dispersion regime at scales below the Rossby radius of deformation and local dispersion in the same scale range. For example, Meyerjürgens et al. (2020) identified significantly different dispersion regimes in the vicinity of the tidal front in the North Sea. Scaling of the relative dispersion indicated a non-local dispersion regime while the Finite Size Lyapunov Exponent (FSLE) showed a local dispersion. At large spatial scales, the existence of different dispersion regimes was revealed. In some studies (e.g., Schroeder et al., 2011), a transition to the diffusive regime was identified in the Liguro-Provençal basin, whereas other studies indicated a Richardson-like dispersion, most likely due to the effect of large-scale velocity shear observed in the Gulf of Mexico (e.g., LaCasce & Ohlmann, 2003). In addition, characterization of the dispersion regime based on the observations from drifting buoys alone is practically difficult and requires many pairs of Lagrangian drifters whose number is always limited in ocean regions. The lack of observations leads to differences in assessment of the dispersion regime in the world oceans (i.e., Haza et al., 2008; Schroeder et al., 2012). Recently, advances in observations of ocean dynamics by remote sensing techniques such as altimetry, coastal radars, etc., and the improvement in the ocean modeling accuracy have opened new opportunities for assessment of the oceanic dispersion properties (using synthetic drifters).

The present study is performed in the Gulf of Tonkin (GoT), a shallow, semi-isolated gulf, located in the northwestern part of the South

China Sea (Fig. 1). As demonstrated in recent studies, the hydrodynamics in the GoT is controlled by the Asian monsoon system, complex bathymetry and exchanges with the South China Sea in the south and through the Hainan Strait (e.g., Tran et al., 2021; Piton et al., 2021; Rogowski et al., 2019). The freshwater input from the Red River impacts the hydrology and circulation along the Vietnamese coast with a strong seasonality as shown recently for instance by Nguyen-Duy et al. (2021). In coastal and shallow-water seas, a combination of tidal and wind forcing, in conjunction with complex topography, can lead to the formation of sub-mesoscale eddies (e.g., Zimmerman, 1981). Additionally, large freshwater discharge enhances the density gradients and can also generate sub-mesoscale motions that play an important role in organizing the flow structures and material transport.

In this work, we employ the realistic, high-resolution numerical model SYMPHONIE and velocity measurements by high-frequency radars to investigate the dispersion properties of the flow field. We adopt an approach based on particle pairs statistics to quantify different scales of the flow field variability and associated dispersion regimes, in the GoT. This article is organized as follows. In section 2, we briefly describe the data and methods used for dispersion quantification. The description of the flow fields during two selected periods is given in section 3. In section 4, results of the assessment of the turbulent dispersion based on the coastal radar velocity measurements and the numerical model simulations are presented. We also assess the effect of river discharge on the Lagrangian statistics. We discuss the results in section 5 and summarize them in section 6.

2. Materials and methods

2.1. HF radar velocity measurements

The velocity data were acquired at two radar sites, Nghi Xuan (XUAN, 105.82 °E, 18.62 °N) and Dong Hoi (DHOI, 106.64 °E, 17.47 °N), which have been operating within the GoT since 2012 (Fig. 1). The radar network was configured to operate at a frequency of 4.625 MHz (which was changed to 5.25 MHz in 2018). The radial velocity component is measured by the radars at the effective depth of ~2 m with an instrumental error of ~0.07 m s⁻¹. The following configuration has been

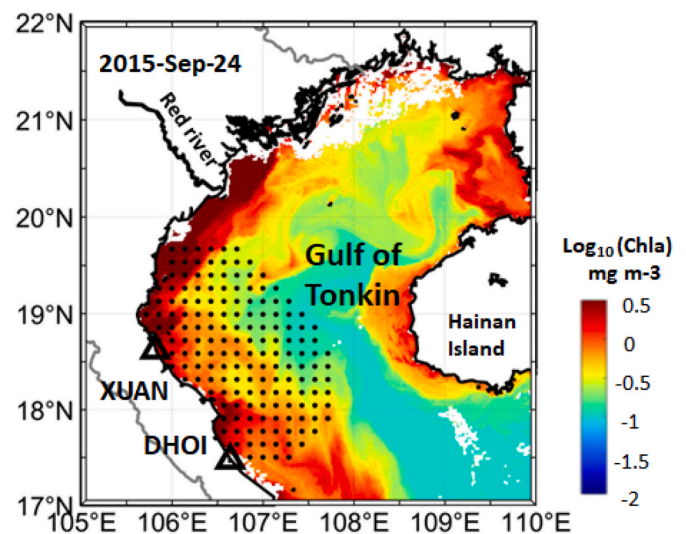


Fig. 1. Study region – the Gulf of Tonkin. Location of HF radars sites is indicated by triangles. Black dots show the radar coverage adopted in the study. The dot spacing is 12 km. Color shading represents a snapshot of Chl-a concentrations (in \log_{10} scale) obtained from the Aqua/MODIS sensor on September 24, 2015. High Chl-a concentration patterns, extending from the nearshore blooming region seaward, are visible through the elongated filaments and small eddies.

used at each radar site to retrieve the radial velocities of the surface currents: 5.8 km along the beam and azimuthal spacing 5° . The temporal resolution was set to 1 h. The HFR total velocities were mapped using EOF/Variational interpolation method (Yaremchuk and Sentchev, 2011). The resulting product consists of hourly maps of two current velocity components (zonal and meridional) on a regular 6-km grid as described in Tran et al. (2021).

2.2. Numerical model configuration

We use the numerical simulations of Nguyen-Duy et al. (2021) made with SYMPHONIE model. SYMPHONIE is a hydrostatic numerical model which solves the primitive equations on a curvilinear bipolar Arakawa C-grid with regular sigma vertical levels (Marsaleix et al., 2006, 2008). A description of the model configuration is given in Nguyen-Duy et al. (2021) and we only recall here the characteristics relevant to this study. The grid covers the whole GoT with a highly variable horizontal resolution, from ~ 300 m along the Vietnamese coast and the Red River delta region, to about 1.5–2 km in the middle Gulf, and reaching the maximum, 4.5 km, at the southern open boundary (see Fig. 2A in Nguyen-Duy et al., 2021). The water column is discretized onto 20 sigma levels.

The bathymetry is reconstructed from GEBCO 2014 combined with other sources and field surveys in order to characterize the complex topography, with many islands and islets located within the region and especially the coastal area adjacent to the Red River delta (Piton et al., 2020). Intertidal areas are simulated with a wetting and drying scheme. The $k-\epsilon$ turbulence closure scheme is implemented as in Michaud et al. (2012).

Tidal motions at the open boundaries are prescribed from the sea surface elevation and barotropic currents of 9 tidal constituents from the FES2014 atlas (Lyard et al., 2021). The tidal astronomical potential is also considered at every grid point of the model. In addition, the $1/12^\circ$ spatial resolution, daily averaged sea surface height (SSH), velocity components, temperature and salinity provided by the Copernicus Marine Systems (CMEMS) global model are also used at the boundaries.

At the sea surface, the boundary conditions include the 3-hourly data for wind, precipitation, solar energy, atmospheric temperature and pressure from the Operational ECMWF product. The fluxes of momentum, heat, and freshwater are computed internally in the model using the bulk formulae of Large and Yeager (2004).

In the reference simulation (hereafter GoT-Ref), the river discharge from 16 rivers is introduced in the model and configured as realistically as possible according to the method described in Nguyen-Duy et al. (2021). Daily freshwater runoff is used from the main seven distributaries of the Red River. For other rivers, climatological data are used. An additional configuration without the river discharge (GoT-noriv configuration, see Nguyen-Duy et al., 2021) is used to assess the effect of rivers discharge on the dispersion properties.

The model was extensively validated over the period 2011–2016 and the results of the validation are given in Piton et al. (2021) and Nguyen-Duy et al. (2021). In our study, we performed an additional comparison of the model simulation with the current velocity derived from HFR measurements for two periods: August and November 2015 (Fig. 2). The correlation between the current velocity derived from both data sources remains larger than 0.7 with a slightly higher value obtained in November (0.85). A relative difference of about 6–10% quantifies the disagreement between the HFR data and the numerical simulations, for both the latitudinal (u) and longitudinal (v) velocity components. The model velocities were found to be slightly smaller than those derived from HFR measurements.

2.3. Lagrangian diagnostics

In this study, we used the velocity data from the model simulation covering one-year long period in 2015. Virtual particles organized in clusters were advected using OceanParcels Lagrangian framework (<https://oceanparcels.org>) by the velocity field from the model at 1 h resolution. These Lagrangian tracers were uniformly distributed in the surface layer at 2 m depth. Each cluster included one center particle and two satellite pairs along x- (longitude) and y-axis (latitude) with the initial separation $\delta_0 = 0.5$ km. The clusters were seeded every 2 km

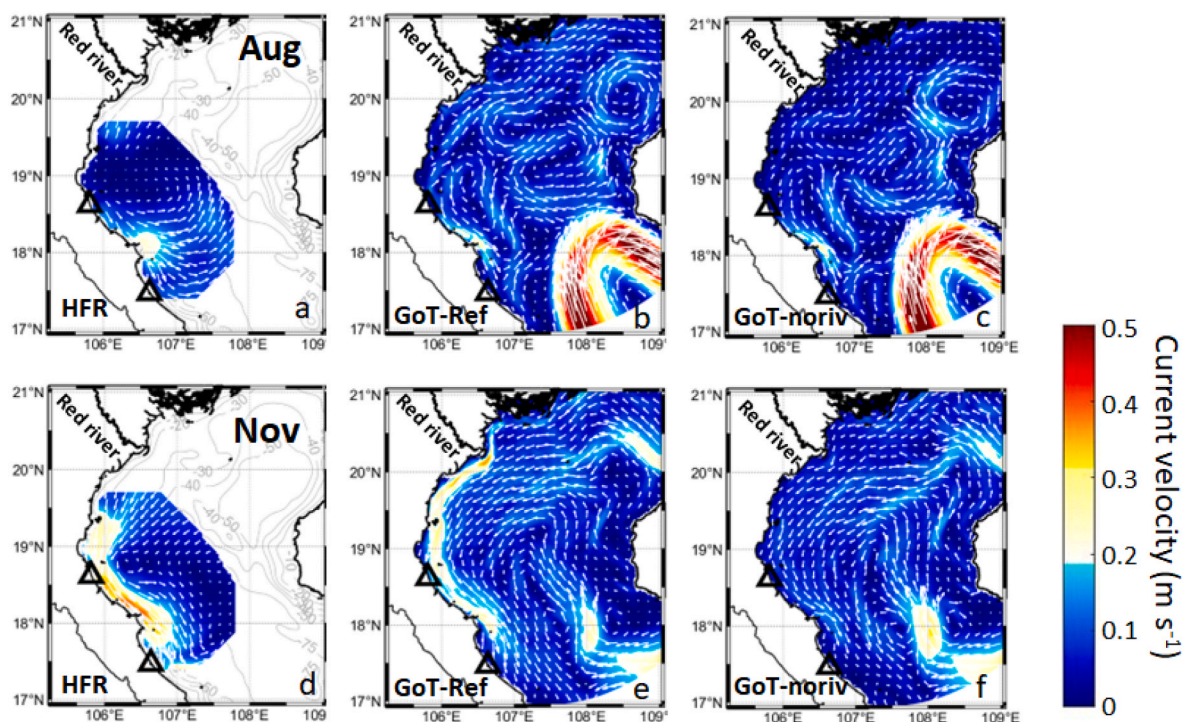


Fig. 2. 30-day mean surface currents in the GoT from HFR measurements (a, d) and numerical model in two configurations: with river discharge (b, e) and without river discharge (c, f) in August and November 2015. The current vectors are interpolated on a regular grid and plotted every 15 km.

across the domain in order to keep the initial pair separation as low as possible and not to exceed a reasonable computational cost. The particles are advected horizontally using the 4th order Runge-Kutta scheme.

In this study, we focus on assessing the statistics of Lagrangian particle pairs advected in the flow fields derived from the HFR measurements and the model simulation during two seasons (summer and late fall). The Lagrangian quantities analyzed include the relative dispersion, relative diffusivity and Finite Size Lyapunov Exponent (FSLE).

The relative dispersion is a common metric for assessing the dispersion of tracers. It is defined as the average, over all particle pairs, of the squared separation between particles i and j in a pair at time t :

$$\delta^2(t) = \frac{1}{N(N-1)} \sum_{ij} \left\| \vec{x}_i(t) - \vec{x}_j(t) \right\|^2 \quad (1)$$

where N is the number of particles. The pairs were identified using the particles with initial separations below 2 km. The relative dispersion behavior depends on the level of turbulence in the flow field. The latter is reflected in the kinetic energy spectrum which shows a power law distribution as a function of the (horizontal) wavenumber $k = |\vec{k}|$: $E(k) \simeq k^{-\beta}$. At the early stage, when the pair separation is small, the particle pair velocities are close and the growth of relative dispersion follows a ballistic behavior, $\delta^2 \sim t^2$. At larger time scales, relative dispersion grows exponentially in the case of non-local dispersion, when $\beta > 3$. Otherwise, if $1 < \beta < 3$, relative dispersion is local and scales as a power law $\delta^2 \simeq \frac{4}{\beta-3} t^{\beta-3}$ (Foussard et al., 2017). Richardson super diffusive regime corresponds to $\delta^2 \sim t^3$ where the pair separation is controlled by eddies with a size similar to the separation distance of particles. When the particle separation reaches scales much larger than the largest characteristic flow scale, the pair velocities are considered uncorrelated. Relative dispersion in this case is expected to scale as $\delta^2 \simeq t$, corresponding to a diffusive behavior.

In addition, we diagnose the relative diffusivity κ , which represents the growth rate of the average squared separation. This quantity is defined as the time derivative of relative dispersion,

$$\kappa = \frac{1}{2} \frac{d\delta^2(t)}{dt} \quad (2)$$

and it can be useful to assess the mixing properties and the corresponding spreading regime. For this purpose, it is often interesting to consider κ as a function of the separation distance δ , rather than of time. Depending on the shape of the given kinetic energy spectrum, $\kappa(\delta)$ scales as δ^2 for the non-local dispersion regime and as $\delta^{4/3}$ (when $\beta = 5/3$) for the local dispersion one.

The third quantity, the Finite Size Lyapunov Exponent (FSLE), is estimated by measuring the time τ , averaged over all particle pairs, needed to separate particles in a pair from a distance δ_k to a distance $\delta_{k+1} = r \delta_k$, with $r > 1$ ($k = 1, \dots, N_k$ and N_k is the number of bins chosen in a way to span the relevant range of scales):

$$\lambda = \frac{\ln(r)}{\tau} \quad (3)$$

Values of FSLE can be used to distinguish a local regime of dispersion from a non-local one (Schroeder et al., 2011). Compared to relative dispersion, the FSLE, being a fixed-length (instead of fixed-time) indicator, better allows to disentangle contributions from turbulent features of different size (Artale et al., 1997). We implemented a method called fastest-crossing for the computation of the FSLE (Lumpkin & Elipot, 2010). A sensitivity study of the results to the choice of r was performed with the fixed number of particles in the area. It was found that varying r from 1.2 to 1.6 does not change the FSLE slope considerably (Poje et al., 2014) and the value of $r = 1.4$ was chosen. The Lyapunov exponent quantifies the exponential rate of separation and is often used for the identification of the non-local regime of pair separation (Haller and Yuan, 2000). At very small separations, the FSLE is expected to recover

such, scale-independent, value. The behavior of the FSLE in a turbulent flow field with spectrum $E(k) = k^{-5/3}$ typically is as follows: $\lambda \simeq \text{constant}$ (exponential growth and non-local dispersion regime) at very small scales, $\lambda \simeq \delta^{-2/3}$ for local dispersion (Richardson regime) in the inertial range and $\lambda \simeq \delta^{-2}$ for the diffusive regime expected at separations much larger than the largest flow scales (Berti et al., 2011; Corrado et al., 2017). A ballistic regime $\lambda \sim \delta^{-1}$ can also be expected in the presence of intense mean currents.

2.4. Horizontal stirring from FSLE maps

In addition, the spatial distribution of FSLEs has been obtained for two selected periods representing two seasons (in August and November). The backward FSLE calculations were performed for 30 days with a time step of 1 h, following the method proposed by d'Ovidio et al. (2004). The advantage of this technique is to restrict the analysis of dispersion within relevant structures among selected length scales. The optimum choice for the spatial FSLE amplification factor δ_f/δ_i was discussed several times in previous studies Haza et al. (2010); Berta et al. (2014). We compute the exponential growth rate, $\lambda(x)$:

$$\lambda(x) = \frac{1}{\tau(x)} \ln \left(\frac{\delta_f}{\delta_i} \right) \quad (4)$$

in analogy with Eq. (3), with $\delta_i \simeq 1.86$ km and $\delta_f = 13$ km. Such values of δ_i and δ_f allow to adequately visualize the relevant coherent structures and transport patterns associated with small-scale processes.

3. Description of the Eulerian flow fields

Fig. 2 shows the 30-days averaged surface current fields from the HF radar measurements and from model simulations in August and November. During summer, the prevailing wind is from the southwest direction and remains persistent until September 12 when a typhoon hits the region. Interestingly, during August, the surface currents from the model show a pronounced northeast flow in the northern part of the gulf above 19°N roughly follows the 50 m isobath. This flow is partly captured in the northern part of the radar field (Fig. 2a). During November, the wind changes to northeasterly with larger speed. The surface currents demonstrate a typical winter pattern with a gulf-scale cyclonic circulation, an intense coastal current in the western part (Fig. 2 d, e), and several energetic jets with mean velocity of 0.3 m s⁻¹. The lack of river discharge in the model leads to the decrease of the surface current velocity (by roughly 0.1 m s⁻¹) in the vicinity of the Red river mouth in August (Fig. 2b and c) and large reduction of the southward coastal jet in November (Fig. 2f).

While the mean current patterns look similar for the three velocity fields, the gradients of the flow field, which control the separation process of the advected Lagrangian particles, appear different. The horizontal flow field and its small-scale content can be inspected from the snapshots of relative vorticity, $\zeta = \frac{\partial v}{\partial x} - \frac{\partial u}{\partial y}$, normalized by the Coriolis frequency f (Fig. 3). A comparison with the Okubo-Weiss parameter, which is also commonly used to quantify the regions dominated by either strain or vorticity reveals that the two quantities are similar (not shown). However, relative vorticity is more suitable to present a larger number of coherent structures of different size in the flow field: from a large-scale structure induced by the incoming current from the open sea that occupies the southern area in August, to abundant thin filaments and small vortices across the gulf with the size from few to tens of km. Additionally, the vorticity distribution in the GoT was compared to the normalized divergence, $\text{div}v/f$, which also controls the separation of drifting particles by enhancing vertical motions and generating clustering effects. Globally, the spatial distribution of both quantities reveals a similarity. However, much weaker values of the divergence field, more affected by noise, make the results difficult to interpret (not shown).

The magnitude of vorticity field shown in Fig. 3 can reach values of

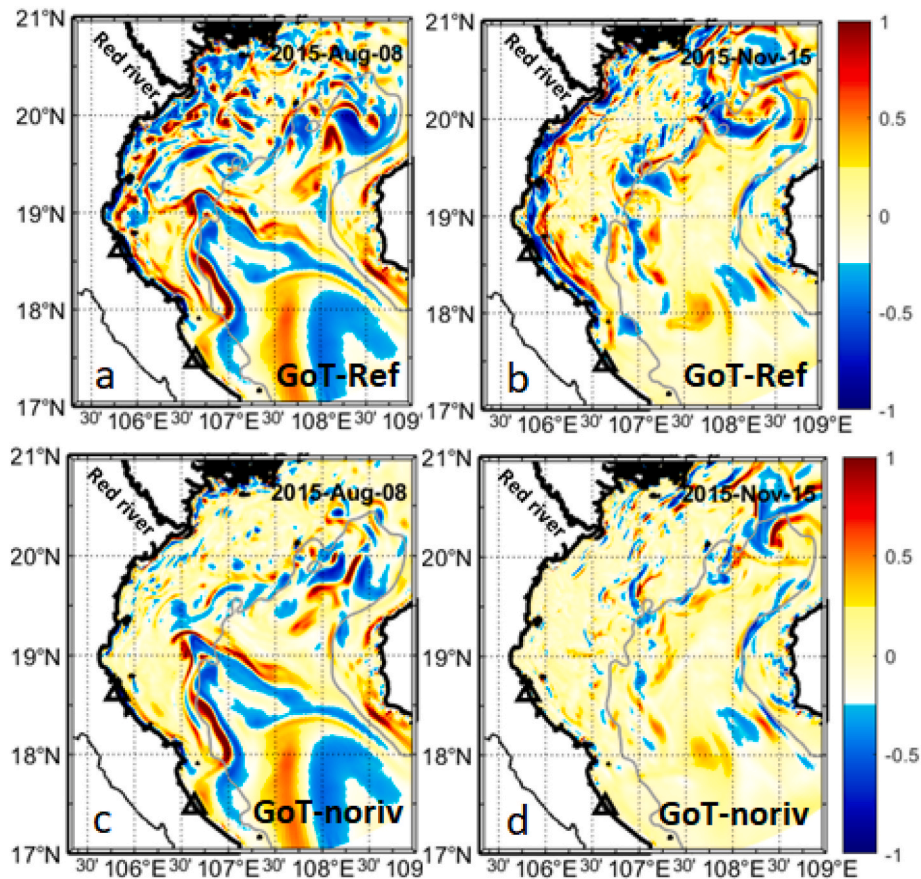


Fig. 3. Snapshots of the relative vorticity normalized by the Coriolis frequency in August and November 2015 from model simulation with (a, b) and without river discharge (c, d). Gray line shows 50 m isobath.

the order of f . When the Rossby number $R_o = \zeta/f \sim O(1)$, a departure from the geostrophic equilibrium in the flow is expected and smaller-scale processes can come into play, such as frontogenesis, mixed-layer instability (Zhong and Bracco, 2013).

Consequently, these sub-mesoscale structures of the velocity fields can directly impact the dispersion process by increasing the rate of dispersion by an order of magnitude compared to the geostrophic turbulence (Berta et al., 2020). A significant difference in velocity gradients between the full model and the model without river discharge is the lack of a number of structures with high vorticity which are observed better in the vicinity of the Red river mouth in August and in November (Fig. 3b, d). Due to the coarse resolution of the HFR measurements, the vorticity field is much smoother, its magnitude is drastically reduced, and small-scale coherent structures are almost vanishing (results not

shown).

The statistical characterization of the velocity field variability can be obtained from the surface turbulent kinetic energy spectrum, $E(k)$ (Fig. 4). The spectra indicate a wide range of motions: from geostrophic and wind driven circulation at large scale to sub-mesoscale turbulent motions. The energy distribution appears different between the two periods and higher for the GoT-Ref model configuration than for the GoT-noriv case. In both models, the kinetic energy is concentrated at large scales (roughly at a length scale of about 60 km) and decays more rapidly (steeper spectral slope $\sim k^{-3}$) at scales below 20 km. In the range roughly above 20 km, despite some noise, the energy distribution follows $k^{-5/3}$ law in both seasons. While the difference in energy distribution between the two seasons is rather small, a significant difference is observed for model simulations with and without river forcing. In the

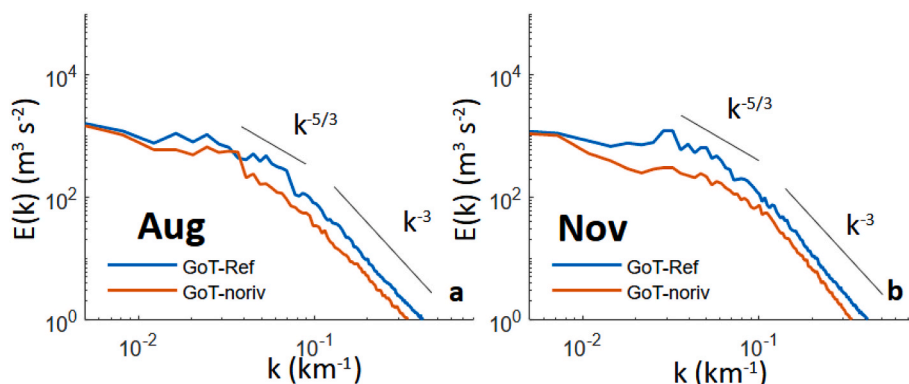


Fig. 4. Power spectra of surface horizontal turbulence kinetic energy in August (a) and November (b) for two model configurations: with and without river input.

latter case, the spectral slope from GoT-noriv model in summer appears steeper in a wide range of scales, 8–70 km, indicating a nonlocal dispersion regime from a Lagrangian perspective (Fig. 4a). In November, the spectrum is flatter and close to the $k^{-5/3}$ law in the scales 10–30 km ($k \sim 0.03\text{--}0.1$), thus suggesting that the dispersion is local and scale dependent (Fig. 4b).

4. Lagrangian pair dispersion

4.1. Lagrangian dispersion from HFR measurements and model simulation

In order to assess the turbulent dispersion in the vicinity of the Vietnamese coast, a first Lagrangian tracking experiment was conducted. A total of 2800 particles were uniformly seeded in a rectangular area of the size $30 \times 30 \text{ km}^2$. Fig. 5 shows the trajectories of particles advected in the velocity field derived from HFR measurements and in the model velocity field. The drifting time of each particle is shown in color. Two releases were performed, one on August 3 and another on November 10, with a tracking time of 30 days. During the first tracking period, the surface currents are driven by the southwest monsoon while during the second period, the winter cyclonic circulation is formed, and the coastal current is reinforced as described in the previous section.

For particles released in August, trajectories are globally controlled by the cyclonic eddy located at the latitude 19°N which “trapped” the particles during the first 10 days. The effect of particle trapping is clearly seen in trajectories from the model and radar velocity fields (Fig. 5a and b). Ten days after the release when the eddy is weakened, particles formed groups drifting in different directions in the model simulations. One group of particles remains within the coastal zone close to XUAN radar site while another group is transported by the coastal buoyant jet southward, down to the gulf entrance (Fig. 5a). The direction of particle advection in the radar-derived velocity field is also southward for days 10–20, then it changes to eastward and northward (Fig. 5b). Agreement

between the two transport patterns is found only for the first 15–20 days of tracking.

In November, a much better agreement in advection pathways in both HFR-derived and model velocity fields is found. In both cases, the trajectories of particles are related to the cyclonic circulation responsible for their transport southward. At the early stages, most of the particles are advected southward by the coastal jet. Later in time (roughly 10 days after the release), the particle drift direction changed to offshore, then reversed to northward after 15 days before continuing to the south after day 20. Regarding the number of particles remaining within the radar coverage area, 30% of particles left the area covered by HF radar measurements while this number is 10% for particles advected by the model velocity fields. The final location of the particles is shown in Fig. 5 in red color. At the end of the 30 days period, the particles advected in the radar velocity field show a more uniform distribution, while in the model simulation, the particles are separated into a number of distant groups (Fig. 5c). It is possible that larger dispersion in the model simulation is caused by irregularities in the velocity fields since the sub-mesoscale motions are better resolved in the high-resolution model. The coarser resolution of radar measurements somehow has an effect on the mean transport and also on the dispersion rate.

To quantify the dispersion regime, we used relative dispersion and the FSLE. In the subsequent analysis of the turbulent dispersion, we used the estimation of the Rossby radius R_d performed by Nguyen-Duy et al. (2021). In summer (April to September), large river discharge and thermal exchange with the atmosphere lead to the increase of stratification and R_d ranges from 10 to 15 km. During winter (Oct to Mar), strong wind and waves increase mixing in the water column. As a consequence, R_d has values of about 4–8 km and is even smaller in the shallow water area (see Fig. 4 in Nguyen-Duy et al., 2021). Therefore, in this study, the value of 8 km in November and 15 km in August are adopted for R_d .

Despite the differences in advection pathways, the relative dispersion regimes appear rather similar (Fig. 6). For the cluster released in

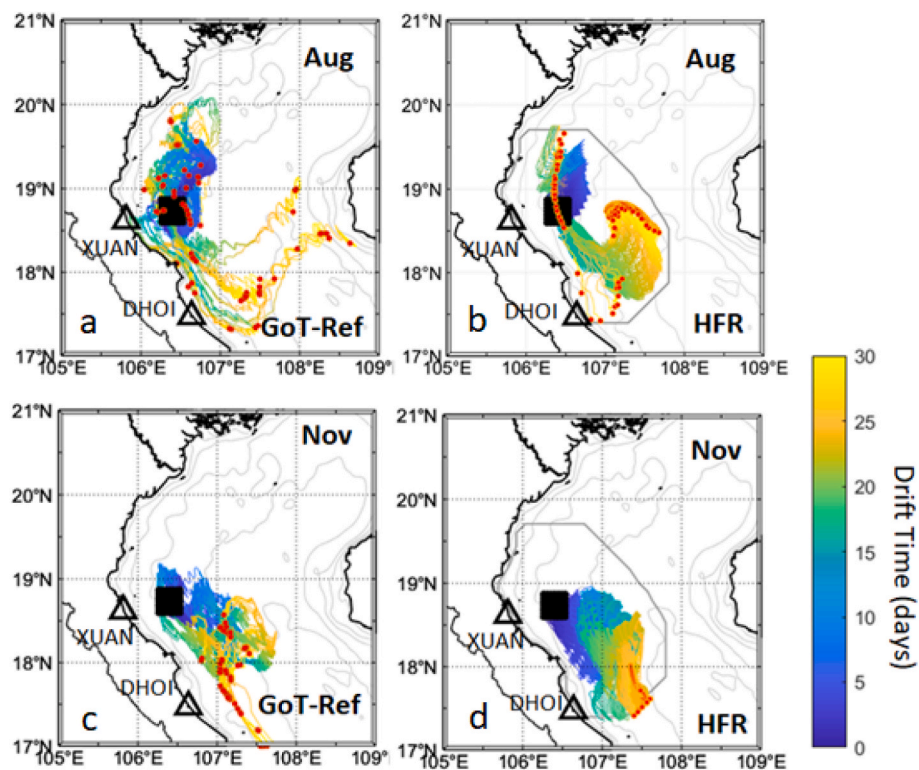


Fig. 5. Trajectories of a subset of particles released close to the XUAN radar site (black square) during both periods of study from the model (a, c) and from the HFR data (b, d) for 30 days since release. The drift time is color-coded. The particle final positions correspond to the red points.

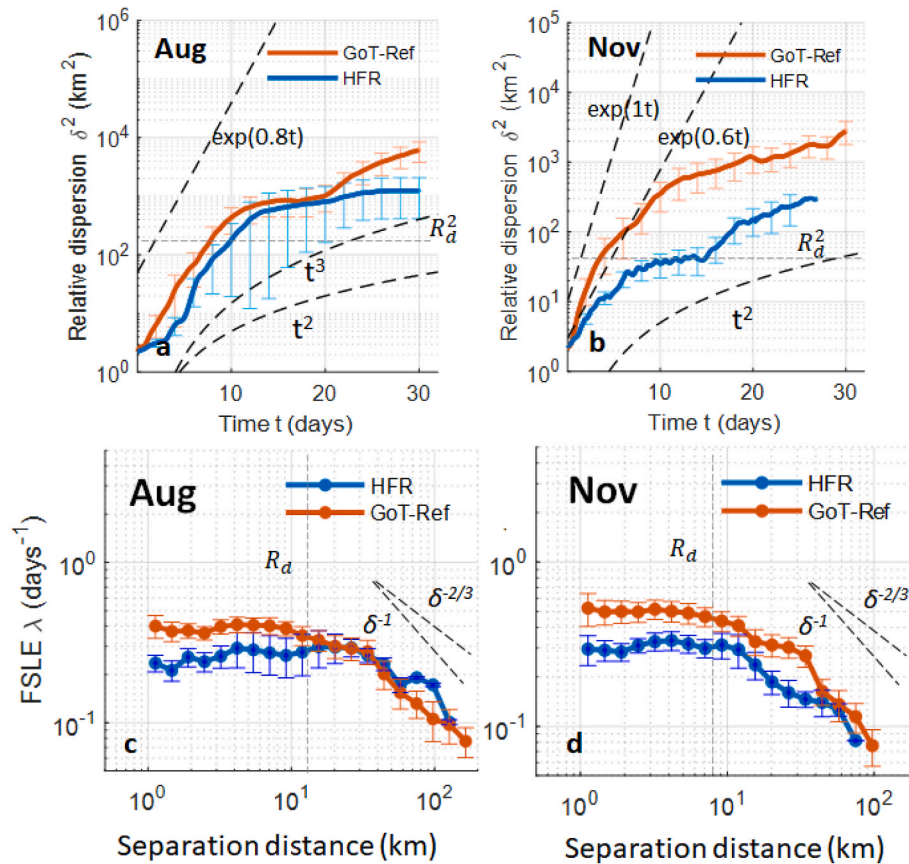


Fig. 6. Scaling properties from relative dispersion (a, b) and FSLE (c, d) for particles advected by model and HFR-derived velocity field in August and November. The horizontal (a, b) and vertical (c, d) lines correspond to separation distances equal to the Rossby radius R_d .

August, for both radar and model fields, relative dispersion indicates an exponential regime ($\exp(0.8t)$) occurring during the first 10 days. It should be noted that in the case of the radar field, the pair separation grows slowly during the first 3 days, which can be explained by the coarser resolution of the HFR measurements (~ 6 km) that is larger than the initial separation (~ 2 km). During the next few days, the dispersion rapidly increases until reaching the distance equal to the grid resolution. The similarity in the exponential growth shown in Fig. 6a for both the HFR and the model indicates that relative dispersion during this initial period is dominated by processes with length-scale larger than the pair separation distance. On day 15, both curves flatten, suggesting that the particle pairs possibly reached eddies with typical length scale of about (20–30) km and larger (at later times). The evolution of relative dispersion follows a power-law behavior not far from Richardson regime for the model ($\delta^2 \sim t^3$) and ballistic regime for the radar ($\delta^2 \sim t^2$). The latter result is affected by larger statistical errors (Fig. 6a).

In November, the relative dispersion shows larger differences (Fig. 6b). Although the particles were released at the coastal current boundary, which can rapidly separate the particles pairs, only the model indicates a high rate of exponential growth ($\exp(t)$). This exponential phase is short and lasts approximately 4 days. Compared to the model, the exponential growth in the HFR measurement is lower. After 10–15 days, both curves display a separation growth that is intermediate between a ballistic (t^2) and Richardson (t^3) regime. The characterization of the separation growth from HFR data is more difficult but, globally, the ballistic regime appears dominant at timescale larger than 4–5 days.

Another approach used for the identification of dispersion regimes involves the FSLE analysis (Fig. 6c and d). The FSLE uses the pair separation distance as an independent variable. Thus, it is less affected by an interfering contribution from pairs evolving under different dispersion regimes at the same time. This methodology, involving HF radar

measurements, has been recently applied by Hernández-Carrasco et al. (2018a, 2018b) to assess dispersion processes in two European coastal regions – the Ibiza channel in the western Mediterranean and in the south-east Bay of Biscay. In agreement with relative dispersion, the FSLE curves demonstrate a non-local dispersion regime for the scale range below 10 km, where the FSLE is constant, $\lambda(\delta) \simeq \lambda_L$, with λ_L the maximum Lagrangian Lyapunov exponent (Fig. 6c and d). In this range, the associated e-folding time ($T = 1 / (2\lambda_L)$) is close to the values found in Fig. 6a, b, i.e., from 1 to 1.25 days in the model and from 1.25 to 1.6 days in the HFR velocity fields. The increase in exponential growth rate in correspondence with increased grid resolution (model vs HFR data) is consistent with previous works (Poje et al., 2010) as pair dispersion at small separation is affected by small-scale motions resolved by the model.

At larger scales, a somewhat common behavior can be recognized. In August, a transition of the dispersion regime is observed at the scale of about 30 km. Above this scale, the FSLE indicates a regime of dispersion close to Richardson one ($\lambda(\delta) \sim \delta^{-2/3}$) for both velocity fields. A similar change of dispersion behavior is observed in November, but now at a scale of roughly 10 km, beyond which the FSLE is somehow steeper than in the Richardson regime and approaches the scaling ($\lambda(\delta) \sim \delta^{-1}$) typical of a ballistic regime.

4.2. Transport and dispersion of particles in the GoT from model simulations

Besides the coarse resolution of the HFR-derived velocity field, another weakness of the HFR measurements is the limited coverage which prevents the assessment of dispersion properties in an area in which the dynamics are strongly dominated by large-scale circulation features (gulf-scale eddy, coastal jet, etc.). Thus, to extend the study area

to the whole region, we resort to numerical simulations. In particular, we are interested in assessing the effect of the river discharge which can rapidly generate sub-mesoscale structures and largely affect the dispersion in the small-scale range. A series of Lagrangian tracking experiments were performed during the same two periods (August and November) with particles seeded uniformly, with a total number of 24065 particles, in the whole domain of model simulation. The average density of particle distribution at the release is 1.25 particles/km². Two model configurations were used to assess the Lagrangian transport: the model with all forcings including the river discharge (GoT-Ref) and without river discharge (GoT-noriv). Fig. 7 shows the spatial distribution of particles 30 days after the release on August 3 (a, c) and November 10 (c, d) and their concentration per km². In all cases, the spatial distribution of particles is found to be controlled by the flow field forced by the monsoon system. The particle distribution reveals a large difference between seasons. In August, the synthetic drifters are scattered throughout the gulf with a high density of particles observed in the middle and the northern gulf, while in November, most of the particles are located in the western gulf (Fig. 7b, d). At the end of the 30-day period, roughly 75% and 90% of particles released in August and November, respectively, remain inside the gulf. This suggests that the hydrodynamics of the gulf is quite local and the exchange with the open sea is limited.

Regarding the impact of the river discharge, the model simulation revealed that the distribution in August is quite similar in the southern gulf, whose dynamics is dominated by the inflow through the southern boundary (Fig. 7a, c). A much larger difference can be seen in the northern gulf. In the GoT-Ref case, the particles are organized into long filaments and wrapped around different eddies. Two regions of high density of particles are found there. The shape of the particle spatial distribution mimics the eddy-like structures with sizes that can reach 100 km. In the GoT-noriv simulation, the spatial distribution of particles in August reveals that mesoscale motions are largely enhanced by the river discharge which increases the number of well-organized structures, such

as eddies and filaments, with large concentration of particles there (Fig. 7a). The results of simulations without river discharge showed that the maximum concentration of particles per km² appears similar but the spatial patterns of particle distribution are less sharp (Fig. 7c).

In November, both models show a large number of elongated structures in particle distribution field. These structures are associated with the unstable manifolds (attracting the materials drifting with currents) and thus structuring the transport of particles. They also indicate a cyclonic pattern in the GoT winter circulation (Fig. 7b, d). Moreover, the particle distribution in both model simulations shows higher concentrations along the middle Vietnamese coast, between 18°–20° N. In the GoT-Ref case, the lines of high-density particle distribution extend toward the south, demonstrating a tendency of particle alignment along the outer edge of the coastal current that carries them southward. In addition to the rapid southward transport, the fluctuation of the jet can facilitate the formation of eddies at the jet boundary, as described via idealized model (Poje et al., 2010) which contribute to the enhancement of particle spreading.

In the GoT-noriv case, the majority of particles are concentrated along a line located roughly 50 km offshore in the northern part and in the southwestern part of the gulf, with large density (~5 particles per km²) observed in the vicinity of the shoreline between latitudes 18°N and 19°N (Fig. 7d).

Fig. 8 helps to characterize the relative dispersion regime in the GoT during the two periods of interest. In August, relative dispersion shows an exponential regime $\exp(0.8t)$ in the GoT-Ref case while it grows a bit more slowly in the GoT-noriv case ($\sim\exp(0.6t)$) (Fig. 8a). A change in dispersion regime occurs after 8 days when the average squared separation exceeds 8 km, a scale close to R_d . The exponential regime indicates non-local dispersion which can be expected at sufficiently small scales, where the flow is smooth. In our case, the separation ($\delta \sim 10$ km) at which dispersion changes behavior is larger than the model resolution. This suggests that dispersion is driven by eddies of larger size, at least of $O(R_d)$. At intermediate times, roughly from 10 days onward,

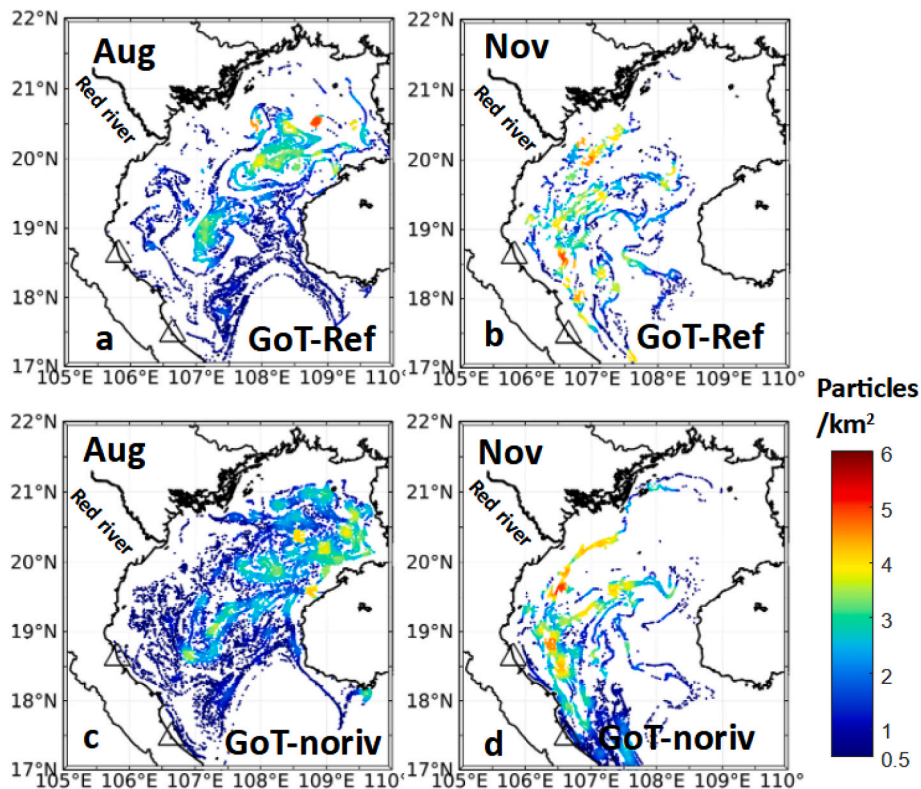


Fig. 7. Particle distribution in August and November, 30 days after the release, from the full model (GoT-Ref) (a, b) and without river discharge (GoT-noriv) (c, d) (unit: number of particles per km²).

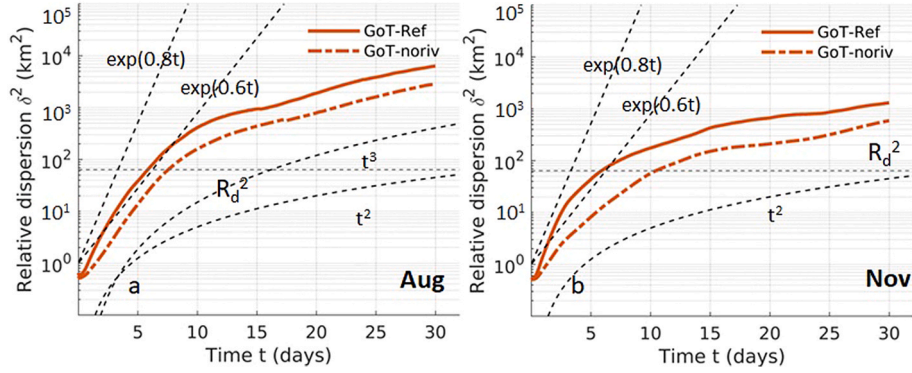


Fig. 8. Relative dispersion as a function of time (in linear-log scale) from the release in August (a) and November (b) in linear-log scale. In this case, particles were released uniformly in the GoT domain. The horizontal line in light black shows a separation distance corresponding to the Rossby radius R_d .

relative dispersion displays a power-law dependency close to a local Richardson regime ($\delta^2 \sim t^3$) at scales larger than 40 km (Fig. 8a).

In November, exponential growth in the GoT-Ref case with a similar rate occurs for a shorter timescale of 3 days (Fig. 8b) then quickly changes to a regime closer to the ballistic ($\delta^2 \sim t^2$) than to Richardson ($\delta^2 \sim t^3$), hinting to particles separating due to the coastal buoyant jet. The ballistic regime holds until the end of the tracking period, when the largest separation of roughly 30 km is reached. The estimated slope for this period is 2.2. In the GoT-noriv case, exponential growth is observed in a short early period, but with a smaller rate ($\sim \exp(0.6t)$). The general features of the evolution of dispersion are not very different from those of the previous cases. The ballistic regime occurs after 5 days of drift. A possible explanation for the change to the ballistic regime in both configurations seems to be related to the particle entrainment inside the coastal current where the velocity shear causes a rapid separation in the cross-jet direction. On the whole, the rate of dispersion in the GoT-Ref case appears larger than that in the GoT-noriv simulation. The difference is caused by the presence of fine motions generated by the river plume advection where particles are stirred more effectively in the area that is not controlled by the mesoscale motions.

Fig. 9 shows relative diffusivity κ as a function of the separation distance δ in August and November respectively. The variability of this quantity is more affected by noise as κ is the time-derivative of relative dispersion. Thus, following Koszalka et al. (2009), we binned $\kappa(\delta)$ in such a way that a given value of δ is a multiple of the previous one, as one would do for the computation of the FSLE. Only the values with more than 50 data points for each bin are considered in the analysis. Despite some wiggles, the scaling properties of κ are consistent with the relative dispersion ones. During August and November, κ scales as δ^2 in the range below R_d . This indicates the dominance of non-local dispersion

at these scales. The transition from the non-local to the local regime ($\kappa \sim \delta^{4/3}$) is observed for scales close to R_d (and in fact slightly smaller). The estimated exponent ranges from 1.2 to 1.5 (Fig. 9), and it is smaller in November. The comparison of diffusivity demonstrates that the freshwater runoff increases the diffusivity in the whole domain.

The FSLE curves λ as a function of δ shown in Fig. 10 reveal a larger difference in dispersion scaling behaviors between the two periods of the study. A common feature for both seasons is a transition from a non-local dispersion regime to a local dispersion one, occurring at a separation distance close to the Rossby radius R_d . The exponential growth of separation distance below R_d gives an e-folding time of 1.2–1.3 days for the GoT-Ref model and 1.7–2.2 days for the GoT-noriv configuration (Fig. 10), in fair agreement with the corresponding estimate obtained from relative dispersion (Fig. 8).

At larger scales (above R_d), a scaling slightly less steep than $\delta^{-2/3}$ and close to $\delta^{-1/2}$ is observed in August, likely due to relatively small-scale coherent structures that steepen the kinetic energy spectrum to k^{-2} (see, e.g., Capet et al., 2008). Note that in the GoT-noriv case the corresponding curve is less steep. Therefore, these results point to the enhancement of the particle spreading at scales comparable or smaller than R_d , in the simulation including the river discharge. The largest difference between the two configurations is observed at small scales. It appears that including the river contributions enhances stirring and shortens the dispersion time by a factor of two in this range of scales (Fig. 10a).

The FSLE curves in November show rather different behavior. Above 20 km, the FSLE in both GoT-Ref and GoT-noriv cases indicates a scale dependent dispersion rate in a broad range of scales. In GoT-Ref case, the FSLE scales as δ^{-1} (ballistic regime) until $\delta \sim 70$ km, which reveals a strong shear dispersion. This can be explained by the tendency of

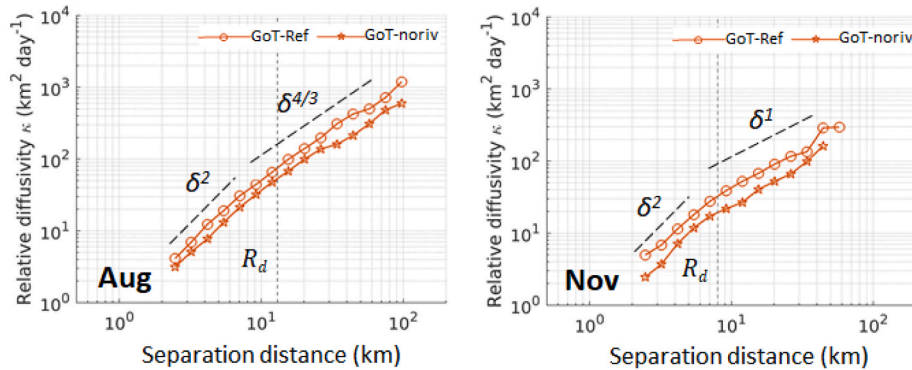


Fig. 9. Relative diffusivity as a function of the separation distance for the two tracking periods in August (a) and November (b) and for the two model configurations (with and without river discharge). In this case, particles were released uniformly in the GoT domain. The vertical lines correspond to separation distances equal to the Rossby radius R_d .

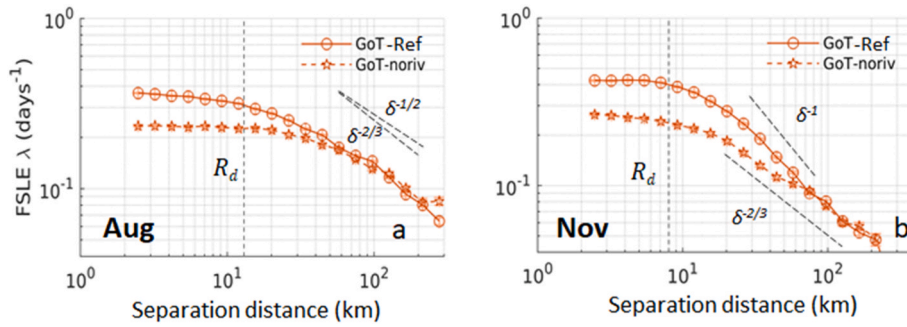


Fig. 10. FSLE $\lambda(\delta)$ versus the separation distance δ in August (a) and November 2015 (b), for particles released uniformly in the GoT domain. The vertical lines correspond to separation distances equal to the Rossby radius R_d .

particles to be concentrated in the western gulf where the coastal current contributes to the rapid southward transport. At scales above 70 km, for both the full model and the GoT-noriv one, the FSLE is perhaps closer to $\delta^{-2/3}$. In the larger scale ranges, the dispersion rate in November is on average slightly lower than in August (Fig. 10b).

4.3. Lagrangian Coherent structures in the GoT

Among different Lagrangian diagnostics, FSLE spatial distributions have been widely used in the analysis of ocean transport and mixing since they can reveal the hidden transport structures of the flow field. The characteristic lines with large FSLE values can show the location of Lagrangian coherent structures (LCS) organizing the transport processes in the GoT. They are sought as the barriers along which the advected particles are concentrated. Here, we analyze FSLE maps after 30 days of backward integration using the model simulation. In Fig. 11, the FSLE distribution is shown for two particular dates, September 02 and

December 10. The figure demonstrates the complexity of the transport and turbulent dispersion. The FSLE fields are organized in thin filament-like features with high values (0.6–1.2 days⁻¹). The LCSs shaped by these lines reveal a frontal zone of 25 km wide along the Vietnamese shore in both periods. Long and highly tangled ridge lines evidence the variability of the flow field there (Fig. 11a). Another region showing a large number of FSLE ridge lines is located further (~100 km) offshore. Most of the ridge lines in this region seem to be aligned along 50 m isobath (Fig. 11b).

In contrast to the full model, the LCSs derived from the GoT-noriv model simulation clearly lack many small-scale features in the coastal region. In addition, they indicate much weaker transport barriers (convergence zones) in the offshore region. FSLE ridge lines appear sparse and characterized by lower values compared to the full model simulation at the same period (Fig. 11c and d).

Each map of FSLE provides information on short-lived processes. The temporal average of the FSLE maps over different periods contains a

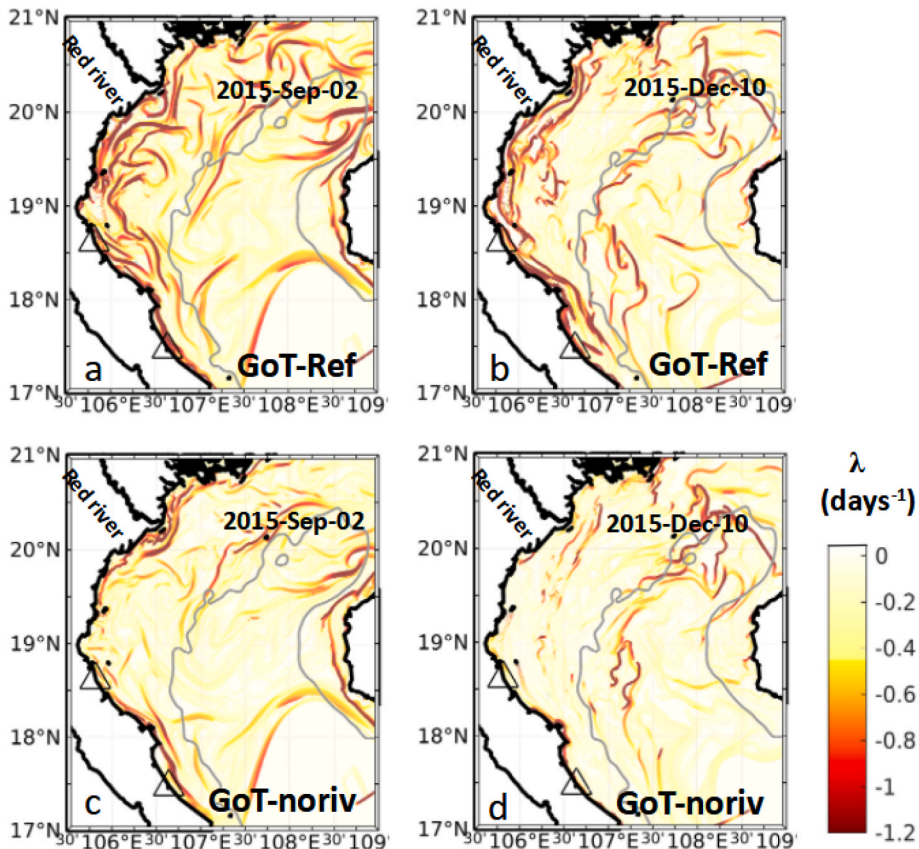


Fig. 11. FSLE distribution for two particular dates on September 02 and December 10 using two model simulations. Gray line shows 50 m isobath.

signature of the low-frequency and longer-lived processes. In addition, such FSLEs provide information on the dispersion time scale. In other terms, the areas with high FSLE values are characterized by more intense horizontal stirring (Hernandez-Carrasco et al., 2012). We assessed the spatial variability of dispersion in the GoT by time averaging thirty FSLE maps for two periods. Several regions of high density of ridge lines can be seen in both seasons with the values of λ ranging from 0.2 to 0.6 days⁻¹. Here we focus on four geographical regions: the northern gulf (A), the southern gulf (B), nearshore (C) and middle gulf region (D). It can be seen that regions of intense dispersion ($\lambda = 0.6$ days⁻¹) are found in the northern gulf (location A) and along the shore (location B), both characterized also by the largest number of filaments and eddies (Fig. 12).

In August, thin ridge lines also indicate an intense dispersion in the north and middle regions (location A and C). Another interesting feature is a quasi-permanent ridge line with $\lambda = 0.6$ days⁻¹ (location B) matching the location of a loop in the flow incoming from the southern boundary (Fig. 2b).

In November, the FSLE maps reveal two regions of intense dispersion located along the middle of the Vietnam coast (region C) and further offshore (region D) with λ ranging from 0.5 to 0.6 days⁻¹. The ridge lines in these two regions indicate the effect of the coastal jet and the branch of the current, originating from Hainan strait (Fig. 2e), on horizontal dispersion. Moreover, spreading of the ridge lines in location D (Fig. 12b) reveals large spatial variability of the dispersion rate within an offshore band of 25–50 km large. LCSs can persist for up to several days thus limiting the exchange between the coastal and offshore regions located west and east of the ridge lines concentrated in sector D (Fig. 12b).

The intensity of stirring, which can be identified by taking the spatial average of the FSLEs over the whole area (d'Ovidio et al., 2004), is approximately 0.4 days⁻¹ in the GoT-ref model. In the absence of the river discharge, the intensity of stirring decreases by roughly two times on average, down to 0.2 days⁻¹. These average values are reasonably in

agreement with the FSLE plateau values λ_L at small scales from Fig. 10.

5. Discussion

In this study, we focus on the analysis of turbulent dispersion regimes and on the identification of LCSs in the GoT from realistic simulations using an approach based on particle pair dispersion. The analysis of relative dispersion is of great importance for the assessment of turbulent stirring in the open and coastal ocean at different spatial and temporal scales. Thus, the main objective of this study was to quantify the turbulent dispersion in the GoT, which is characterized by complex and multiscale dynamics, modulated by the monsoon wind and large buoyant input from a number of rivers (the largest being from the Red River). To the best of our knowledge, this problem has not been addressed yet in this region. Recent advances in the realism of the coastal modeling and observations using coastal radars allow the investigation of the turbulent dispersion using synthetic drifters advected in the radar and model velocity fields. Analysis of turbulent dispersion is performed for two periods, August and November 2015, representing typical summer and winter weather and river discharge conditions. Compared to other velocity data such as geostrophic currents from AVISO products, HFR measurements provide a near-real time, higher space-time resolution (6 km resolution, hourly data compared to roughly 27 km spatial resolution, daily data from AVISO). These data are more suitable for the quantification of the dispersion processes in the GoT. Our results indicate that relative dispersion statistics derived from the HFR tracking of particles are comparable to those obtained from the model. However, the spatial resolution of the HFR-derived velocity fields is still low compared to that of the model. As the short time and small-scale dispersion are sensitive to the details of the flow field, the coarse resolution of the HFR data makes the exploration of small-scale features difficult. In the small-scale range, the dispersion rate estimated from the radar measurements is significantly lower than the one from the model simulations in November (e-folding

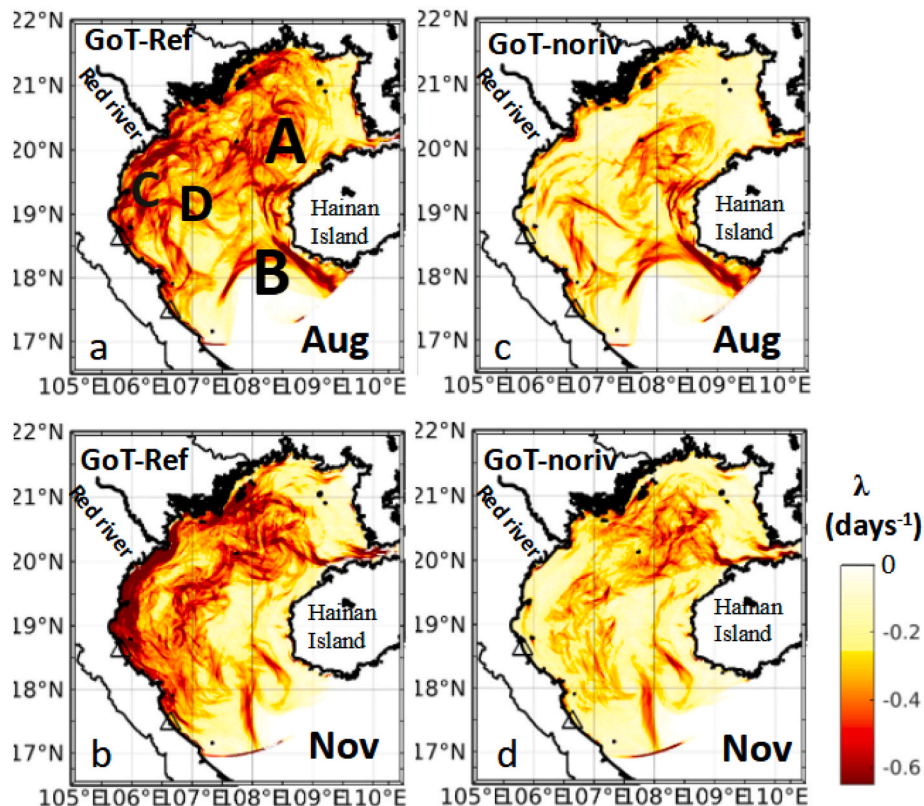


Fig. 12. 30-day mean FSLEs for the period of August and November from the two model simulations: GoT-Ref (a, b) and GoT-noriv (c, d).

time of approximately 2 and 1 days, respectively).

Analysis of relative dispersion, relative diffusivity and FSLE from the numerical model indicated an exponential regime at sub-mesoscale which is consistent with estimations of these quantities for other ocean basins (Beron-Vera and LaCasce, 2016; Berti et al., 2011; Essink et al., 2019; van Sebille et al., 2015). At this scale, the e-folding time estimated using the relative dispersion and the FSLE is similar for both seasons but appears strongly dependent on the river runoff (e-folding time of roughly 1.25 days for the full model and 2.5 days in the GoT-noriv model simulation). At larger scales, the dispersion exhibits a scale-dependent behavior indicative of either Richardson local dispersion or ballistic separation, controlled by strong mean currents. Such a transition between regimes occurs at scales close to the Rossby radius of deformation. In general, the pair dispersion properties in the GoT, obtained from the analysis of three Lagrangian diagnostics (relative dispersion, relative diffusivity and FSLE), are consistent with the results of previous studies, based on the analysis of the global drifter dataset (Corrado et al., 2017).

It is argued that a super diffusive regime can occur in the presence of strong shear and is characterized by the power law behavior ($\gamma > 1$), as reported in some other studies performed in different regions: in the Adriatic Sea, γ is found ~ 1.8 (Haza et al., 2008), in the Gulf of California, $\gamma \sim 1.9$ (Zavala Sansón, 2015). In our case, γ is found larger, ~ 2.2 . However, rather clear hints to Richardson regime ($\gamma = 3$) are also found over some scale subranges for both model configurations, with and without river discharge.

In regions characterized by strong sub-mesoscale dynamics, different limiting FSLE values were found for scales $\delta < 10$ km: λ_L , $\sim 1-1.1$ days $^{-1}$ in the Gulf of Mexico, (Choi et al., 2017), or $\lambda_L \sim 0.6$ days $^{-1}$ in the Liguro basin (Schroeder et al., 2011). In the Gulf of La Spezia, the value of λ_L can readily reach 2.5 days $^{-1}$ (Haza et al., 2010). In our case, the value of λ_L for the same scales ($\delta < 10$ km) is clearly weaker, ranging from 0.3 to 0.4 days $^{-1}$. In addition, the FSLE slopes, both from the radar data and the model, do not show a scale-dependent dispersion regime in the sub-mesoscale range, typically O(1–10 km), which is different from the one found in the well-known regions of strong sub-mesoscale dynamics such as in Ibiza channel (Hernández-Carrasco et al., 2018a) or the Gulf of Mexico (Choi et al., 2017; Poje et al., 2014). This indicates that the contribution of sub-mesoscale motions in turbulent dispersion in the Gulf of Tonkin is weak. This seems reasonable because the GoT is a quite shallow basin with limited potential energy which can be stored in the mixed layer where small eddies can be hashed by the wind. Our results are in agreement with some previous studies, which reported and demonstrated that dispersion at the sub-mesoscale can be induced non-locally by mesoscale motions (e.g., Haza et al., 2008; Poje et al., 2010). However, it should be noted that the variable model resolution, ranging from 0.3 km near the shore to 1.5–2 km in the middle gulf, likely prohibits the exploration of the local stirring generated by small-scale turbulent motions. Assuming that the effective scale of motions resolved in the model is roughly between four to six times the numerical grid resolution, only the upper range of sub-mesoscale variability (scale 1.5–10 km) can be properly identified and assessed. In this regard, HFR measurements in the GoT, with spatial resolution of 6 km, do not allow quantification of surface current velocity variability and dispersion at sub-mesoscale. Moreover, it was demonstrated by Hernández-Carrasco et al. (2018b) that different current mapping techniques, used in radar data processing, can affect the characterization of dispersion regimes based on particle pair statistics.

The impact of the river discharge on the surface dynamics of the GoT is explored using the model simulation with and without rivers runoff. During both periods considered, the river input in the model enhances the dispersion in a wide range of scales, from sub-mesoscale up to 50 km. The river discharge causes a significant change of e-folding time, which decreases from roughly 2.5 days to 1.25 days. The river discharge (when introduced in the model) creates buoyancy gradients and enhances the sub-mesoscale dynamics which in turn modifies the Lagrangian

statistics. However, the difference between two numerical experiments, with and without river discharge, was not found to significantly alter the dispersion scaling behaviors. A possible reason could be that we examined statistics averaged over all particle pairs in the whole domain, while the river discharge primarily enhances the dispersion of particles in the western part of the gulf.

Lastly, we quantified the horizontal stirring caused by small-scale motions using the spatial distribution of FSLEs in different seasons. The LCSs, identified from backward FSLEs using the model velocity field, were analyzed to assess the horizontal stirring by small-scale processes, and appear to be very sensitive to the river forcing. Moreover, the FSLE maps clearly show the regionality of small-scale motions and their impact on dispersion processes. In August, a large concentration of FSLE ridge lines is found in the northern gulf and in the southern gulf where the transport and dispersion are strongly influenced by the incoming flow from the southern open boundary. During August, when the river discharge is at its peak, the river plume is driven northward and can detach from the coast due to the persistent southwest wind (Nguyen-Duy et al., 2021). The surface layer is then decoupled from the subsurface layer. This creates favorable conditions for the development of sub-mesoscale motions via roll-up instabilities of larger scale structures (Klein et al., 2011; Roulet et al., 2012; Berti and Lapeyre, 2021). Alternatively, sub-mesoscale motions could be also generated by a complex topography in the northern gulf (small islands, complex bathymetry, etc.). This can explain a high concentration of large FSLE values in the vicinity of the Red river in the GoT-Ref model (location C in Fig. 12a). In winter, the spatial distribution of FSLEs reveals the existence of another region of high concentration of FSLE ridge lines matching the outer limit of the coastal current which strongly affects the dispersion processes by organizing the particle distribution.

6. Summary

Relative dispersion in the coastal ocean environment, characterized by a wide range of scales of flow variability is still largely unknown. At scales less than a few km, the dispersion processes have been experimentally investigated using surface drifters in a number of limited size coastal regions. The experimental assessment of turbulent dispersion at larger scales is difficult to realize due to the cost of such experiments. In the present study, we adopted an alternative approach and investigated the turbulent dispersion and transport pathways in the GoT by using a large number of virtual drifters advected in the velocity fields derived from a high-resolution numerical model and HFR measurements.

For both types of fields, the results revealed a high degree of consistency regarding the dispersion regime at scales larger than 20 km. At smaller scales, the dispersion rate in the radar velocity field appeared two times lower, which is explained by the comparatively low spatial resolution of radar measurements.

The Rossby radius of deformation, R_d , is a key lengthscale that separates the regimes of turbulent dispersion. It was estimated from numerical simulations in the GoT performed by Nguyen-Duy et al. (2021). Our results revealed a non-local dispersion regime at scales below R_d and local dispersion at larger scales, which is in agreement with the results of earlier investigations performed in different regions of the world oceans (e.g., Haza et al., 2008; Corrado et al., 2017).

The seasonal variability in transport patterns and dispersion regimes was further characterized. The time evolution of dispersion showed an exponential growth during the first 5–8 days of drift for both seasons, followed by a power law regime during the next 6–20 days. The ballistic regime was found to dominate the dispersion at mesoscales in winter while Richardson super diffusion regime was diagnosed in summer. This change in regime is mainly related to a combined effect of river discharge and summer monsoon wind which enlarges the river plume area and enhances stirring in the coastal region extending up to 100 km offshore. In November, the ballistic regime is probably induced by strong northeastern monsoon wind providing the coastal current

strengthening and local shear dispersion intensification. The local dispersion regime (in the sub-mesoscale range) was not clearly identified, suggesting that the mesoscale circulation in the GoT largely governs the dispersion at small scales.

Four regions with high level of dispersion were identified in the GoT: a nearshore region under the fresh-water influence, an offshore region distant by ~100 km from the coast, a central part of the northern gulf, and a region close to the southern gulf entrance. Seasonality in dispersion strength caused by the variability of wind forcing and freshwater input from the Red river were identified and quantified.

Finally, this study provided a reference for further analysis of turbulent dispersion regimes in this geographic region, poorly covered by observations. It highlighted the capability of high-resolution model in reconstructing the circulation patterns and assessing the impact of the monsoon wind and river runoff on turbulent dispersion and transport of passive tracers. This is of primary importance for applications involving multi-scale interactions in the coastal ocean, the transport of particulate biological or anthropogenic material.

Authors' contributions

M.C.T, A.S, S.B contributed to the conception and scientific design of the study. M.C.T performed the data analysis and wrote the original version of the manuscript. A.S, S.B and N.A were deeply involved in the analysis, manuscript organization, and co-writing. N.A and T.ND developed and provided the numerical model results. All authors actively contributed to the revision of the manuscript.

Funding

This study was funded by the Université du Littoral-Côte d'Opale and the Région "Hauts-de-France" PhD fellowship.

Declaration of competing interest

The authors declare that they have no known competing financial interests or personal relationships that could have appeared to influence the work reported in this paper.

Acknowledgments

This study was supported by the University of Littoral Côte d'Opale and the Région "Hauts-de-France" PhD fellowship. Chl-a data were provided by ACRI, GlobColour products (<https://hermes.acri.fr/>). We would like to thank Tran Trung Kien for help with Chl-a data processing. The SYMPHONIE code is available at the SIROCCO French national service website (<https://sirocco.obs-mip.fr/>). CALMIP facilities (Toulouse, France) were used to run the model. We acknowledge the anonymous Reviewers for the constructive comments which helped to improve the scientific quality of the paper.

References

- Artale, V., Boffetta, G., Celani, A., Cencini, M., Vulpiani, A., 1997. Dispersion of passive tracers in closed basins: beyond the diffusion coefficient. *Phys. Fluids* 9 (11), 3162–3171. <https://doi.org/10.1063/1.869433>.
- Beron-Vera, F.J., LaCasce, J.H., 2016. Statistics of simulated and observed pair separations in the Gulf of Mexico. *J. Phys. Oceanogr.* 46 (7), 2183–2199. <https://doi.org/10.1175/JPO-D-15-0127.1>.
- Berta, M., Ursella, L., Nencioli, F., Doglioli, A.M., Petrenko, A.A., Cosoli, S., 2014. Surface transport in the Northeastern Adriatic Sea from FSLE analysis of HF radar measurements. *Continental Shelf Res.* 77, 14–23. <https://doi.org/10.1016/j.csr.2014.01.016>.
- Berta, M., Griffa, A., Haza, A.C., Horstmann, J., Huntley, H.S., Ibrahim, R., Lund, B., Özgökmen, T.M., Poje, A.C., 2020. Submesoscale kinematic properties in summer and winter surface flows in the Northern Gulf of Mexico. *J. Geophys. Res.: Oceans* 125 (10). <https://doi.org/10.1029/2020JC016085>.
- Berti, S., Lapeyre, G., 2021. Lagrangian pair dispersion in upper-ocean turbulence in the presence of mixed-layer instabilities. *Phys. Fluids* 33 (3), 036603. <https://doi.org/10.1063/5.0041036>.
- Berti, S., Dos Santos, F.A., Lacorata, G., Vulpiani, A., 2011. Lagrangian drifter dispersion in the Southwestern Atlantic Ocean. *J. Phys. Oceanogr.* 41 (9), 1659–1672. <https://doi.org/10.1175/2011JPO4541.1>.
- Capet, X., McWilliams, J.C., Molemaker, M.J., Shchepetkin, A.F., 2008. Mesoscale to submesoscale transition in the California current system. Part I: flow structure, eddy flux, and observational tests. *J. Phys. Oceanogr.* 38, 29–43. <https://doi.org/10.1175/2007JPO3671.1>.
- Choi, J., Bracco, A., Barkan, R., Shchepetkin, A.F., McWilliams, J.C., Molemaker, J.M., 2017. Submesoscale dynamics in the Northern Gulf of Mexico. Part III: Lagrangian implications. *J. Phys. Oceanogr.* 47 (9), 2361–2376. <https://doi.org/10.1175/JPO-D-17-0036.1>.
- Corrado, R., Lacorata, G., Palatella, L., Santoleri, R., Zambianchi, E., 2017. General characteristics of relative dispersion in the ocean. *Sci. Rep.* 7 (1), 46291. <https://doi.org/10.1038/srep46291>.
- d'Ovidio, F., Fernández, V., Hernández-García, E., López, C., 2004. Mixing structures in the Mediterranean Sea from finite-size Lyapunov exponents. *Geophys. Res. Lett.* 31 (17), 1–4. <https://doi.org/10.1029/2004GL020328>.
- D'Asaro, E.A., Shcherbina, A.Y., Klymak, J.M., Molemaker, J., Novelli, G., Guigand, C. M., Haza, A.C., Haus, B.K., Ryan, E.H., Jacobs, G.A., Huntley, H.S., Laxague, N.J.M., Chen, S., Judt, F., McWilliams, J.C., Barkan, R., Kirwan, A.D., Poje, A.C., Özgökmen, T.M., 2018. Ocean convergence and the dispersion of flotsam. *Proc. Natl. Acad. Sci. USA* 115 (6), 1162–1167. <https://doi.org/10.1073/PNAS.1718453115>.
- d'Ovidio, F., Della Penna, A., Trull, T.W., Nencioli, F., Pujol, M.-I., Rio, M.-H., Park, Y.-H., Cotté, C., Zhou, M., Blain, S., 2015. The biogeochemical structuring role of horizontal stirring: Lagrangian perspectives on iron delivery downstream of the Kerguelen Plateau. *Biogeosciences* 12 (19), 5567–5581. <https://doi.org/10.5194/bg-12-5567-2015>.
- Essink, S., Hormann, V., Centurioni, L.R., Mahadevan, A., 2019. Can we detect submesoscale motions in drifter pair dispersion? *J. Phys. Oceanogr.* 49 (9), 2237–2254. <https://doi.org/10.1175/JPO-D-18-0181.1>.
- Foussard, A., Berti, S., Perrot, X., Lapeyre, G., 2017. Relative dispersion in generalized two-dimensional turbulence. *J. Fluid Mech.* 821, 358–383. <https://doi.org/10.1017/jfm.2017.253>.
- Haller, G., Yuan, G., 2000. Lagrangian coherent structures and mixing in two-dimensional turbulence. *Phys. Nonlinear Phenom.* 147 (3–4), 352–370. [https://doi.org/10.1016/S0167-2789\(00\)00142-1](https://doi.org/10.1016/S0167-2789(00)00142-1).
- Haza, A.C., Poje, A.C., Özgökmen, T.M., Martin, P., 2008. Relative dispersion from a high-resolution coastal model of the Adriatic Sea. *Ocean Model.* 22 (1–2), 48–65. <https://doi.org/10.1016/j.ocemod.2008.01.006>.
- Haza, A.C., Özgökmen, T.M., Griffa, A., Molcard, A., Poulain, P.-M., Peggion, G., 2010. Transport properties in small-scale coastal flows: relative dispersion from VHF radar measurements in the Gulf of La Spezia. *Ocean Dynam.* 60 (4), 861–882. <https://doi.org/10.1007/s10236-010-0301-7>.
- Haza, A.C., Özgökmen, T.M., Hogan, P., 2016. Impact of submesoscales on surface material distribution in a gulf of Mexico mesoscale eddy. *Ocean Model.* 107, 28–47. <https://doi.org/10.1016/j.ocemod.2016.10.002>.
- Hernandez-Carrasco, I., López, C., Hernandez-García, E., Turiel, A., 2012. Seasonal and regional characterization of horizontal stirring in the global ocean. *J. Geophys. Res.: Oceans* 117 (10), 1–12. <https://doi.org/10.1029/2012JC008222>.
- Hernández-Carrasco, I., Orfila, A., Rossi, V., Garçon, V., 2018a. Effect of small scale transport processes on phytoplankton distribution in coastal seas. *Sci. Rep.* 8 (1), 1–13. <https://doi.org/10.1038/s41598-018-26857-9>.
- Hernández-Carrasco, I., Solabarrieta, L., Rubio, A., Esnaola, G., Reyes, E., Orfila, A., 2018b. Impact of HF radar current gap-filling methodologies on the Lagrangian assessment of coastal dynamics. *Ocean Sci.* 14 (4), 827–847. <https://doi.org/10.5194/os-14-827-2018>.
- Klein, P., Lapeyre, G., Roulet, G., Le Gentil, S., Sasaki, H., 2011. Ocean turbulence at meso and submesoscales: connection between surface and interior dynamics. *Geophys. Astrophys. Fluid Dyn.* 105 (4–5), 421–437. <https://doi.org/10.1080/03091929.2010.532498>.
- Koszalka, I., LaCasce, J.H., Orvik, K.A., 2009. Relative dispersion in the Nordic Seas. *J. Mar. Res.* 67 (4), 411–433. <https://doi.org/10.1357/002224009790741102>.
- LaCasce, J.H., 2008. Statistics from Lagrangian observations. *Prog. Oceanogr.* 77 (1), 1–29. <https://doi.org/10.1016/j.pocean.2008.02.002>.
- LaCasce, J.H., Ohlmann, C., 2003. Relative dispersion at the surface of the Gulf of Mexico. *J. Mar. Res.* 61 (3), 285–312. <https://doi.org/10.1357/002224003322201205>.
- Lacroix, G., Maes, G.E., Bolle, L.J., Volckaert, F.A.M., 2013. Modelling dispersal dynamics of the early life stages of a marine flatfish (*Solea solea* L.), pp. 13–25. <https://doi.org/10.1029/2010JC006338>. *J. Sea Res.* 84, 13–25.
- Large, W.G., Yeager, S., 2004. Diurnal to Decadal Global Forcing for Ocean and Sea-Ice Models: The Data Sets and Flux Climatologies. NCAR Technical Note, NCAR/TN-460 +STR. Boulder, CO: National Center for Atmospheric Research. <https://doi.org/10.5065/D6KK98Q6>.
- Lumpkin, Rick, Elipot, Shane, 2010. Surface drifter pair spreading in the North Atlantic. *J. Geophys. Res.* 115 (c12). <https://doi.org/10.1029/2010JC006338>.
- Lyard, F.H., Allain, D.J., Cancet, M., Carrère, L., Picot, N., 2021. FES2014 global ocean tide atlas: design and performance. *Ocean Sci.* 17 (3), 615–649. <https://doi.org/10.5194/os-17-615-2021>.
- Marsaleix, P., Auclair, F., Estournel, C., 2006. Considerations on open boundary conditions for regional and coastal ocean models. *J. Atmos. Ocean. Technol.* 23 (11), 1604–1613. <https://doi.org/10.1175/JTECH1930.1>.
- Marsaleix, P., Auclair, F., Floor, J.W., Herrmann, M.J., Estournel, C., Pairaud, I., Ules, C., 2008. Energy conservation issues in sigma-coordinate free-surface ocean models. *Ocean Model.* 20 (1), 61–89. <https://doi.org/10.1016/j.ocemod.2007.07.005>.

- Meyerjürgens, J., Ricker, M., Schakau, V., Badewien, T.H., Stanev, E.V., 2020. Relative dispersion of surface drifters in the North Sea: the effect of tides on mesoscale diffusivity. *J. Geophys. Res.: Oceans* 125 (8). <https://doi.org/10.1029/2019JC015925>.
- Michaud, H., Marsaleix, P., Leredde, Y., Estournel, C., Bourrin, F., Lyard, F., Mayet, C., Arduin, F., 2012. Three-dimensional modelling of wave-induced current from the surf zone to the inner shelf. *Ocean Sci.* 8 (4), 657–681. <https://doi.org/10.5194/os-8-657-2012>.
- Nguyen-Duy, T., Ayoub, N.K., Marsaleix, P., Toubanc, F., De Mey-Frémaux, P., Piton, V., Herrmann, M., Duhaut, T., Tran, M.C., Ngo-Duc, T., 2021. Variability of the Red River Plume in the Gulf of Tonkin as revealed by numerical modeling and clustering analysis. *Front. Mar. Sci.* 8, 1636. <https://www.frontiersin.org/article/10.3389/fmars.2021.772139>.
- Piton, V., Ouillon, S., Vinh, V.D., Many, G., Herrmann, M., Marsaleix, P., 2020. Seasonal and tidal variability of the hydrology and suspended particulate matter in the Van Uc estuary, Red River, Vietnam. *J. Mar. Syst.* 211, 103403. <https://doi.org/10.1016/j.jmarsys.2020.103403>.
- Piton, V., Herrmann, M., Marsaleix, P., Duhaut, T., Ngoc, T.B., Tran, M.C., Shearman, K., Ouillon, S., 2021. Influence of winds, geostrophy and typhoons on the seasonal variability of the circulation in the Gulf of Tonkin: a high-resolution 3D regional modeling study. *Reg. Stud. Mar. Sci.* 45, 101849. <https://doi.org/10.1016/j.rsma.2021.101849>.
- Poje, A.C., Haza, A.C., Özgökmen, T.M., Magaldi, M.G., Garraffo, Z.D., 2010. Resolution dependent relative dispersion statistics in a hierarchy of ocean models. *Ocean Model.* 31 (1–2), 36–50. <https://doi.org/10.1016/j.ocemod.2009.09.002>.
- Poje, A.C., Özgökmen, T.M., Lipphardt, B.L., Haus, B.K., Ryan, E.H., Haza, A.C., Jacobs, G.A., Reniers, A.J.H.M., Olascoaga, M.J., Novelli, G., Griffa, A., Beron-Vera, F.J., Chen, S.S., Coelho, E., Hogan, P.J., Kirwan, A.D., Huntley, H.S., Mariano, A.J., 2014. Submesoscale dispersion in the vicinity of the Deepwater Horizon spill. *Proc. Natl. Acad. Sci. U.S.A.* 111 (35), 12693–12698. <https://doi.org/10.1073/pnas.1402452111>.
- Rogowski, P., Zavala-Garay, J., Shearman, K., Terrill, E., Wilkin, J., Lam, T.H., 2019. Air-sea-land forcing in the Gulf of Tonkin: assessing seasonal variability using modern tools. *Oceanography* 32 (2), 150–161. <https://doi.org/10.5670/oceanog.2019.223>.
- Roulet, G., McWilliams, J.C., Capet, X., Molemaker, M.J., 2012. Properties of steady geostrophic turbulence with isopycnal outcropping. *J. Phys. Oceanogr.* 42 (1), 18–38. <https://doi.org/10.1175/JPO-D-11-09.1>.
- Sansón, L.Z., Pérez-Brunius, P., Sheinbaum, J., 2016. Surface relative dispersion in the Southwestern Gulf of Mexico. *J. Phys. Oceanogr.* 47 (2), 387–403. <https://doi.org/10.1175/JPO-D-16-0105.1>.
- Schroeder, K., Haza, A.C., Griffa, A., Özgökmen, T.M., Poulain, P.M., Gerin, R., Peggion, G., Rixen, M., 2011. Relative dispersion in the Liguro-Provençal basin: from sub-mesoscale to mesoscale. *Deep Sea Res. Oceanogr. Res. Pap.* 58 (3), 209–228. <https://doi.org/10.1016/j.dsr.2010.11.004>.
- Schroeder, K., Chiggiato, J., Haza, A.C., Griffa, A., Zgkmen, T.M., Zanasca, P., Molcard, A., Borghini, M., Poulain, P.M., Gerin, R., Zambianchi, E., Falco, P., Trees, C., 2012. Targeted Lagrangian sampling of submesoscale dispersion at a coastal frontal zone. *Geophys. Res. Lett.* 39 (11), 4–9. <https://doi.org/10.1029/2012GL051879>.
- Tran, M.C., Sentshev, A., Nguyen, K.C., 2021. Multi-scale variability of circulation in the Gulf of Tonkin from remote sensing of surface currents by high-frequency radars. *Ocean Dynam.* 71 (2), 175–194. <https://doi.org/10.1007/s10236-020-01440-x>.
- van Sebille, Erik, Beal, Lisa M., Johns, William E., 2011. Advective time scales of Agulhas Leakage to the North Atlantic in surface drifter observations and the 3D OFES model. *J. Phys. Oceanogr.* 41 (5), 1026–1034. <https://doi.org/10.1175/2010JPO4602.1>.
- van Sebille, E., Waterman, S., Barthel, A., Lumpkin, R., Keating, S.R., Fogwill, C., Turney, C., 2015. Pairwise surface drifter separation in the western Pacific sector of the Southern Ocean. *J. Geophys. Res.: Oceans* 120 (10), 6769–6781. <https://doi.org/10.1002/2015JC010972>.
- Yaremchuk, M., Sentshev, A., 2011. A combined EOF/variational approach for mapping radar-derived sea surface currents. *Continental Shelf Res.* 31 (7–8), 758–768. <https://doi.org/10.1016/j.csr.2011.01.009>.
- Zavala Sansón, L., 2015. Surface dispersion in the Gulf of California. *Prog. Oceanogr.* 137, 24–37. <https://doi.org/10.1016/j.pcean.2015.04.008>.
- Zhong, Y., Bracco, A., 2013. Submesoscale impacts on horizontal and vertical transport in the Gulf of Mexico. *J. Geophys. Res.: Oceans* 118 (10), 5651–5668. <https://doi.org/10.1002/jgrc.20402>.
- Zimmerman, J.T.F., 1981. Dynamics, diffusion and geomorphological significance of tidal residual eddies. *Nature* 290 (5807), 549–555. <https://doi.org/10.1038/290549a0>.